Journal of
Materials Chemistry A

PAPER

View Article Online
View Journal | View Issue

Check for updates

Cite this: *J. Mater. Chem. A*, 2025, **13**, 36564

One-step dual process strategy for holey graphite towards scalable and stable lithium-ion battery anodes

Keerti Rathi, †*[a] Viktoriya Pakharenko,†[a] Otavio Augusto Titton Dias, [a] Colin van der Kuur,[c] Ning Yan [b] and Mohini Sain*[a]

Received 7th July 2025
Accepted 26th September 2025

DOI: 10.1039/d5ta05487g

rsc.li/materials-a

Our research demonstrates a one-step dual-process acid treatment approach for modifying graphite, which increases its interlayer distance and generates nanoscale holes, thereby effectively shortening the lithium-ion diffusion pathway without the need for heteroatom doping. Compared with pristine graphite (PG), the expanded holey graphite (EG) produced by this process achieves significantly enhanced electrochemical performance while maintaining structural integrity. The EG shows excellent electrochemical performance, reaching a specific capacity of 179.45 mAh g^{-1} and retaining 89.3% of its capacity after 300 cycles in a full pouch cell combined with a commercial NMC523 cathode. High coulombic efficiency (approximately 93.8%) and improved cycling stability confirm the durability of the etched graphite. Beyond mere performance considerations, the study elucidates the degradation mechanisms inherent in commercial lithium-ion batteries (LIBs), thereby offering dependable guidance for electrode surface engineering and the optimization of cycling protocols. With this scalable and impurity-free approach to modification, purified etched graphite emerges as a promising candidate for next-generation LIB anodes, satisfying the high energy requirements and durability necessary for electric vehicles and advanced energy storage systems.

1 Introduction

The rapid development in energy storage technologies and the global transition to renewable energy have significantly increased the demand for high-performance lithium-ion batteries (LIBs), particularly for applications in electric vehicles (EVs), grid storage, and portable electronics.[1–3] Despite their commercial success, largely due to their energy density, long cycle life, and stable operation, LIBs face critical challenges under certain conditions. For instance, low temperatures and rapid charging can result in problems such as low-capacity retention, thermal instability, and lithium plating, which affect longevity and safety.[1] Researchers are investigating innovative materials and design approaches, such as sophisticated electrode designs,[4,5] novel electrolyte formulations, and enhanced separator technologies, to address these concerns.[6]

Due to these challenges, the complex interplay at the anode-electrolyte interface[8] has emerged as the key (critical) focus because of the direct influence on the lithium-ion transport, SEI formation, and overall battery performance under demanding conditions. Similar interfacial issues have been reported in other battery chemistries (Zn, Na, ammonium-ion *etc.*), where electrolyte additives improved interface stability,[7] defect engineering in 2D materials enhanced ion storage,[8] and rational interface design governed by thermodynamic and kinetic descriptors stabilized hetero-metallic interfaces.[9] These cross-chemistry insights underscore the universal importance of interfacial engineering, directly motivating the development of surface-modified graphite approaches for LIBs.

A wide range of materials has been explored as LIB anodes, but graphite remains the most widely adopted due to its favourable intercalation chemistry, high electrical conductivity, chemical stability, and low working potential *versus* Li/Li^+.[6,10] Its theoretical capacity (~372 mAh g^{-1}) is also competitive with that of many alternative materials.[11,12] However, the redox potential of graphite is close to the potential for lithium metal plating.[13–15] Under demanding conditions such as a high state of charge (SOC), high C-rate, or low temperature, this potential can drop below the plating threshold due to increased overpotential and polarization. Furthermore, raw or recovered graphite often contains surface impurities, binder residues, and structural defects, which hinder electrochemical performance. These imperfections not only reduce electrochemical performance but also exacerbate lithium plating, capacity fade, and safety risks,

---

[a] *Department of Mechanical and Industrial Engineering, University of Toronto, Toronto, ON, M5S 3G8, Canada. E-mail: keerti.rathee1989@gmail.com; m.sain@utoronto.ca*

[b] *Department of Chemical Engineering & Applied Chemistry, 200 College Street, Toronto, ON, M5S 3E5, Canada*

[c] *Zentek Ltd, 24 Corporate Court, Guelph, ON, N1G 5G5, Canada*

† These authors contributed equally to this work.

particularly under fast-charging or low-temperature operation.[16–19], Recent studies further highlight that conventional graphite anodes suffer from sluggish Li^+ diffusion kinetics and unstable solid-electrolyte interphase (SEI) evolution in such conditions.[8] Consequently, impurity removal and interfacial optimization have emerged as critical strategies to suppress lithium plating, stabilize cycling performance, and extend anode lifetime.[9]

To extend the performance and lifespan of lithium-ion batteries, researchers have explored a wide range of pre-treatment strategies for graphite. These include modifying the surface and internal structure, increasing the interlayer spacing, creating defects through doping, enhancing porosity, or applying protective coatings.[20,21] More recently, efforts have focused on alloying graphite with elements such as silicon[22–24] or incorporating metal oxides and heteroatoms to boost capacity and minimize degradation. While these approaches show promise, they often come with trade-offs, including complex fabrication steps, higher costs, mechanical instability due to volume changes, and lower initial coulombic efficiency. Despite the promise of these composites, pure graphite remains the preferred material for commercial applications due to its simplicity, reliability, and cost-effectiveness.[21]

Among the various pre-treatment techniques, acid leaching has emerged as one of the most effective approaches for both graphite purification and performance enhancement. Treatments using mineral acids (*e.g.*, HCl, HNO_3, H_2SO_4)[25–32] and organic acids (*e.g.*, acetic or citric acid)[33,34] have shown promising results in removing metal impurities, expanding interlayer spacing, and introducing oxygen-containing functional groups.[26] These modifications increase the electrolyte wettability, lithium-ion diffusion, and promote the formation of a stable solid electrolyte interphase (SEI), thereby improving both capacity and rate performance.[5] For example, Natarajan *et al.*[33] reported that acetic acid-treated graphite delivered 328 mAh g^{-1} over 150 cycles with 88.6% retention.

Acid treatments induce significant structural changes, such as partial exfoliation, the formation of porous networks, and the creation of defects. These features increase lithium-ion accessibility and contribute to higher overall storage capacity.[6] Previous studies using acids such as H_2SO_4, HF, and HCl, as well as alkalis like NaOH, have shown limited effectiveness.[27] For instance, Sulfuric acid may leave behind crystalline sulphate residues due to its low volatility, which can disrupt SEI formation and increase the side reactions on the anode surface. Similarly, hydrochloric acid (HCl)[25] offers a much milder oxidative environment, which may result in insufficient surface functionalization. This limits electrolyte wettability and lithium-ion intercalation, and residual chloride ions pose a risk of corrosion to metallic current collectors. Treatments involving mixed acids such as HNO_3 and H_2SO_4 are particularly aggressive and often lead to over-functionalization, excessive porosity, and partial exfoliation of graphite layers.[26] Although such treatments may enhance initial capacity, they often come at the cost of reduced cycling stability and reduced first-cycle coulombic efficiency.

Nitric acid (HNO_3) is highly effective due to its strong oxidative nature. It introduces oxygen-containing functional groups (–COOH, –OH, and amine). These groups contribute to defect formation, interlayer spacing expansion, and enhanced electrolyte wettability during the pre-carbonization phase, thereby improving lithium intercalation kinetics.[10] Hydrogen peroxide (H_2O_2) further enhances the process as a strong oxidizer, assisting in breaking down contaminants and promoting exfoliation. We developed a two-step chemical approach that combines HNO_3 and H_2O_2 for acid treatment, followed by alkaline leaching with NH_4OH. This dual-stage process offers several benefits compared to traditional single-step treatments. The HNO_3/H_2O_2 system provides deep oxidative cleaning and activates the surface, removing both organic and metallic contaminants while creating holes and pores in the carbon matrix through oxidative etching. Subsequently, NH_4OH leaching effectively removes any remaining metal ions and neutralizes acidic surface groups, ultimately improving electrochemical stability. Following chemical modification, thermal carbonization removes most of the unstable carboxyl groups, but retains more robust oxygen-containing functionalities (C=O, C–O). These residual groups, along with the defects created during initial functionalization, maintain polar sites that improve Li^+ transport and SEI formation. Overall, the process promotes microstructural rearrangement, controlled defect formation, and uniform pore distribution, enhancing electrolyte accessibility and lithium-ion transport.

Compared to earlier methods, our approach produces holey graphite with enhanced lithium-ion diffusion during charge–discharge, while maintaining a cost-effective and scalable synthesis process. Furthermore, unlike aggressive treatments that can cause excessive oxidation and damage the structure, our controlled acid–base process maintains the crystalline structure while improving surface functionality. These advantages make our method well-suited for real-world applications, particularly in the scalable recycling and regeneration of LIB anodes.

Our broader aim was to support the development of next-generation LIBs that combine high performance with improved safety and environmental sustainability. Specifically, we focused on reducing ion diffusion distances and promoting stable SEI layer formation through carefully controlled acid etching and alkaline leaching. In this study, we proposed a facile synthesis route based on HNO_3 and H_2O_2 etching, followed by NH_4OH leaching. This approach expanded the interlayer spacing of graphite and facilitated more efficient lithium intercalation/de-intercalation during charge–discharge cycles. Nitric acid treatment introduced functional groups such as amine, which enhance lithium-ion transport. By selectively targeting reactive edge sites and the delocalized π-electron system of graphite, our combined HNO_3–H_2O_2 treatment enabled the control of defect formation and surface activation, contributing to enhanced electrochemical performance.

2 Methodology

2.1 Surface modification of graphite

The EG was synthesized through an etching treatment using a mixture of nitric acid (HNO_3) and hydrogen peroxide (H_2O_2). PG (6.0 g) was added to HNO_3 (1.0 M, 75 mL) and stirred for approximately 30 minutes. Then, H_2O_2 (1.0 M) was added dropwise to the solution in a 1 : 1 v/v ratio, and the mixture was transferred to a round-bottom flask fitted with a reflux condenser. The slurry was stirred and refluxed at 100 °C for 3 hours. To observe the effect of the etching process over time, the treatment duration varied from 40 minutes to 24 hours. Shorter periods (less than 1 hour) caused moderate etching without clear morphological changes. Longer exposures (3 hours) increased porosity and surface activation; however, very lengthy treatments (24 hours) resulted in significant morphological alterations and made it difficult to remove the acid from the graphite (as confirmed by pH monitoring). This etching of graphite negatively impacted the anode during electrochemical cycling by encouraging side reactions and reducing stability.

After cooling to room temperature, NH_4OH (28–30%) was added dropwise to neutralize and leach residual acids while maintaining a pH of 8.0–8.5 for about 30 minutes. The solid was collected *via* vacuum filtration, washed with deionized water, and vacuum-dried at 120 °C overnight. Finally, the dried sample was carbonized at 900 °C under a nitrogen atmosphere for 1 hour to remove labile carboxylic groups. After the acid treatment, ICP-OES analysis was conducted to determine the remaining impurities, as illustrated in Fig. 1.

2.2 Anode slurry preparation

A mixture of active and carbon black (1 wt% of active material) was ball-milled for 30 minutes at 700 rpm to assess the electrochemical performance. Then, water (120 wt% of active material) was heated to 80 °C, and CMC (2.25 wt% of active material) was slowly added into the heated water while stirring until fully dissolved, which usually takes ~60 minutes. Thereafter, SBR (2.25 wt% of active material) was added to the CMC solution and stirred for another 60 minutes. Next, the active material and conductive materials were added to the slurry and stirred for 2 hours. The viscosity of the final slurry was approximately 5500 CPS.

2.2.1 Materials characterization. The crystalline structure of electrode materials was characterized using a Philips P.W. 1830 powder X-ray diffractometer with a Cu Kα-ray source, scanning from 10° to 80°. Microstructure and morphology were examined using a JSM-6610LV SEM and a QUANTA FEG 250 scanning electron microscope equipped with energy-dispersive X-ray spectroscopy (EDS). X-ray photoelectron spectroscopy (XPS) on a PerkinElmer Phi 5500 ESCA spectrophotometer probed the chemical and electronic states of the surface. High-resolution transmission electron microscopy (HRTEM) was performed with a Hitachi HF3300 Environmental-CFE-TEM operated at a voltage of 300 kV. HRTEM images were analyzed using ImageJ software. The Brunauer–Emmett–Teller (BET) analysis for surface area and pore size was determined by N_2 adsorption/desorption measurements (Quantachrome Nova 1200 Analyzer) following sample degassing under vacuum at 150 °C for 2 h. The Thermo Scientific iCAP Pro ICP-OES provides rapid, simultaneous measurement of multiple elements, and can view the plasma either axially or radially.

2.2.2 Pouch cell assembly and battery testing protocols. Each slurry was cast onto a 10 μm copper foil for the anode using a doctor blade with a slit width of 45 μm and dried in an oven at 60 °C for 24 hours. The dried slurry was further compressed with a roll press for consistent thickness. The

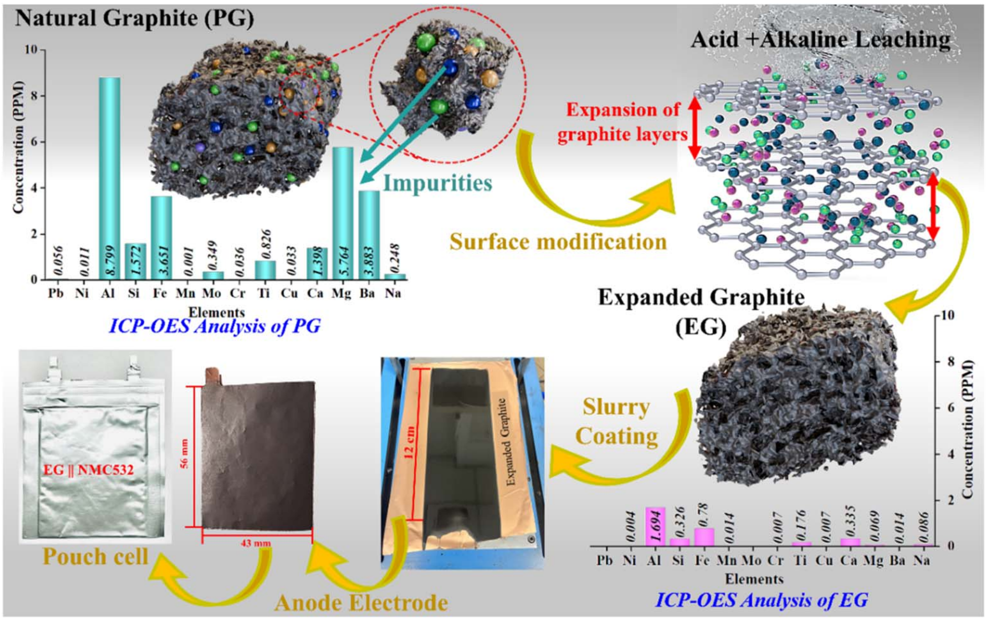

Fig. 1 Schematic diagram showing the preparation of expanded holey graphite (EG) from pristine graphite (PG) and its pouch cell assembly.

anode sheet was then cut using an electrode-cutting machine. The anode, cathode, and separator were alternately stacked, with two or more single-sided anode/cathode pieces as the outer layers. Nickel and aluminium cell terminals were welded onto the anode and cathode electrodes, respectively, using ultrasound. The cut electrodes were placed in a vacuum for 2 hours at 60 °C and then transferred to the glove box. The electrodes and electrolytes were housed in aluminium-laminated film. The sides were sealed using a sealing machine, and 1.5 mL of 1.0 M $LiPF_6$ in EC/DEC = 50/50 (v/v) electrolyte was added to the top of the pouch cell. Finally, the top was vacuum sealed. After assembly, the cells underwent a formation cycle by charging and discharging at a 0.5C-rate.

During the aging, the battery was aged by charging at a 0.5C rate from 2.5 to 4.3 V and immediately discharging from 4.3 V to 2.5 V. Furthermore, there was no relaxation time between the charge and discharge processes. Galvanostatic charging and discharging profiles for the fabricated pouch cells were obtained using an 8-channel battery Analyzer (MTI, USA) with a cut-off voltage range set at 2.0–4.3 V. The state of health (SOH) was determined according to the discharge capacity. Cyclic voltammetry (CV) plots and electrochemical impedance spectroscopy (EIS) were conducted on an Admiral Instruments Squidstat Plus potentiostat. Half-cells featuring Li metal as the counter electrode were employed for EIS analyses. EIS curves were obtained under open circuit potential, in a frequency range of 2 MHz–0.1 Hz, with an excitation potential of 5 mV and 20 points per decade.

2.3 Disassembly of an aged pouch cell

Following the cycling test outlined above, the aged and fresh cells were discharged to 2.5 V at a constant current rate. Subsequently, they were meticulously disassembled within a glove box filled with argon. To prevent cross-contamination, the extracted negative electrodes were washed separately with diethyl carbonate (DEC) for 10 minutes and then dried in the glove box for 48 hours.

3 Results and discussion

3.1 Morphology and structural analysis

The XRD analysis of pristine natural graphite (PG) and expanded etched graphite (EG) is presented in Fig. 2. The XRD pattern of PG exhibits a sharp peak at 26.7° and 54.8°, corresponding to the (002) and (004) planes, respectively. The (002) plane indicates the interplanar spacing and high crystallinity of the graphite. After surface treatment, the peak shifts to a lower angle at 26.15°, confirming an increase in the *d*-spacing of EG to 0.342 nm, compared to that of PG (0.335 nm), as illustrated in the enlarged part of Fig. 2. This shift is attributed to a reduction in particle size, confirmed by BET analysis, due to the intercalation of oxygen-containing functional groups at the edges, such as carboxyl groups and epoxides.[35] These oxygen functionalities actively promote the formation of a dry-coordinated state between Li^+ and lone-pair electrons of oxygen atoms, thereby enhancing lithium intercalation across the interface during charging.

From the XRD data, it is observed that PG also has the sp^3 hybridized carbon phase, which is confirmed by the peaks at 43.8°, 50.7°, and 74.5°, corresponding to (111), (202), and (220) planes, respectively.[36,37] sp^3 hybridized carbon is typically an electrical insulator and does not exhibit weak van der Waals forces between layers,[38] which prevents electron transfer and restricts the movement of lithium ions within the structure, a necessary condition for efficient battery operation. However, surface-modified EG has more sp^2 carbon structure, which is confirmed by diminishing the sp^3-hybridized covalent bond. Thus, the surface modification is to make the highly stable sp^2-hybridized graphite and increase the interplanar spacing, which helps to improve the lithium-ion movement within the expanded graphite.

The resulting data from the BET (Brunauer–Emmett–Teller) experiment show the increase in the surface area of graphite from 4.1 $m^2 g^{-1}$ to 7.9 $m^2 g^{-1}$ after the acid treatment of pristine graphite, as shown in Fig. 2(b) and (c). In pristine graphite (PG), the pore size distribution is primarily concentrated in the 2–5 nm range, indicating the presence of small mesopores and a relatively limited surface area. In contrast, acid-etched graphite (EG) shows a broader pore size distribution, with a significant shift toward larger pores in the 5–10 nm range. This structural change results in a significant increase in surface area. The enhancement of porosity and surface area in EG confirms that acid etching effectively increases the pore size of the graphite structure, thereby creating more accessible interaction sites. It promotes the improvement of material performance during cycling by improving cycle stability and change transfer efficiency.[39] The analysis indicates that the increased porosity improves electrolyte wettability, promoting better electrochemical reactions and Li-ion flow cycles.[40]

SEM evaluation reveals the morphological change of EG from PG, as shown in Fig. 3(a). It shows the tightly packed graphitic flakes of PG. The chemical treatment of PG, which transformed into EG, shows a smaller flake size with multilayers and mild delamination. The results of this analysis indicate that the use of surface engineering is responsible for higher crystallization.

The high-resolution TEM images and SAED pattern were used to investigate in depth the microstructure of graphite after etching treatment, which clearly demonstrates the chemically modified graphite crystallinity and confirms the increment in interplanar spacing. Fig. 3(b) shows that EG has a small hole apart from the PG; it might be because of oxidizing acid and H_2O_2 etchant generate oxygenated defects, interlayer gases expand and burst out, and selective etching removes carbon atoms at defect-rich sites (see Fig. S5). This synergistic process creates porous, holey graphite with shortened Li^+ diffusion paths. In pristine graphite, two hybridized carbon phases are observed. However, in expanded graphite, only sp^2-hybridized carbon is present, confirming the purity of the graphite structure. The enhanced lattice spacing and stable structure are further validated by FFT and SAED patterns. The measured lattice spacing of 0.335 nm and 0.202 nm corresponds to the

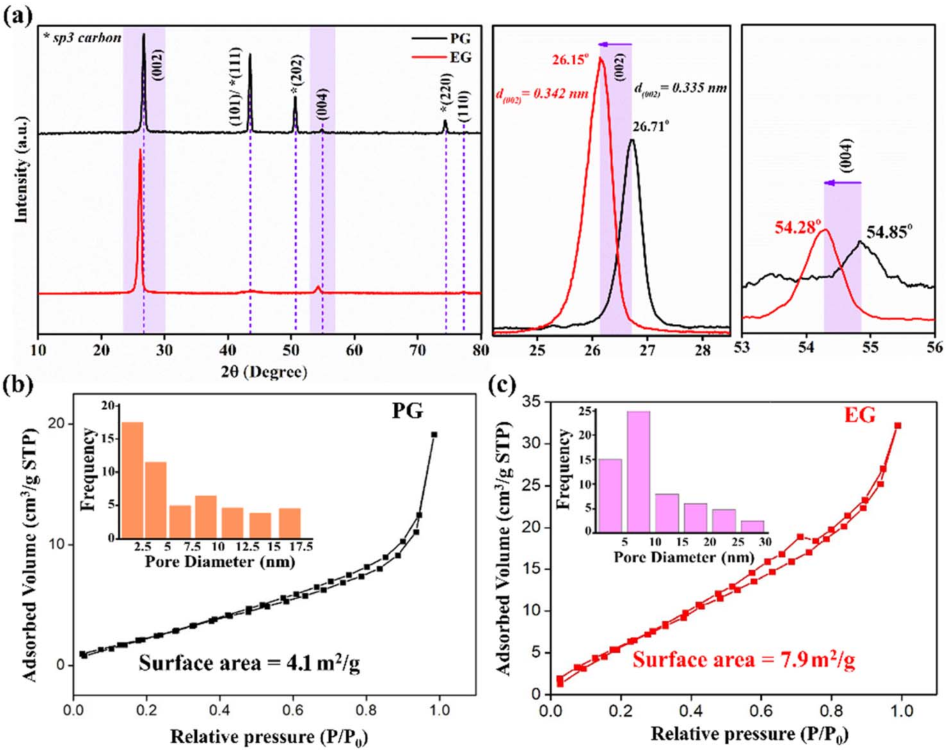

Fig. 2 (a) Comparative study of XRD and (b, c) BET analysis (pore diameter-overlay image part) of PG and EG.

(002) and (111) planes, respectively, which are confirmed by the FFT of PG. After expansion, the (002) plane's spacing increases to approximately 0.349 nm, indicating structural modification.

Based on these results, expanded graphite (EG) exhibits a porous structure where the activity at the edge sites is significantly higher than at the surface. This enhanced porosity provides abundant active sites for Li-ion storage, making it a promising material for an anode.

3.2 Battery performance analysis

The EIS analysis of pristine graphite and expanded etched graphite has been conducted using a half-cell up to 20 cycles, as shown in Fig. 4(a) and (b). The Nyquist plots show the resistance of the solution resistance (R_s) in the electrolyte, the solid electrolyte interphase resistance (R_{sei}), and charge transfer resistance (R_{ct}), which represent the electrochemical and interfacial properties of PG and EG before and after 20th cycling (Table 1).[41]

The solution resistance (R_s), which represents the ionic conductivity of the electrolyte and any associated resistance at the electrode–electrolyte interface, demonstrated notable differences between PG and EG. For PG after cycling, indicating potential electrolyte degradation or changes in the electrode–electrolyte interface over the cycling process. This is further supported by XPS data, which reveals an increased amount of carbonate derivatives on the graphite surface after cycling.

For EG, R_s also increased slightly after cycling, suggesting minor electrolyte decomposition or changes at the electrode–electrolyte interface. However, compared to PG, the relatively small rise in R_s for EG indicates that its porous and expanded structure facilitates electrochemical reactions with lower resistance and enhances structural stability, ensuring efficient ionic transport throughout the electrode.[42] The consistently low R_s of EG before and after cycling highlight its improved electrolyte penetration and ion transport properties, contributing to its superior electrochemical performance.

The resistance of the solid electrolyte interphase (R_{sei}) showed a similar increasing trend for both materials, though the extent and underlying mechanisms differ significantly. For PG, the R_{sei} increased significantly after cycling. This increase indicates substantial growth or modification of the SEI layer during the cycling process, possibly due to the formation of a thicker and less uniform SEI caused by continuous electrolyte decomposition.[43] Before cycling, the SEI formation on EG is minimal due to its large surface area and abundant active sites, leading to negligible initial resistance. After cycling, the formation of a more substantial and stable SEI layer on the expanded and porous structure increases R_{sei} slightly, though it remains significantly lower than that of PG. The enhanced surface area of EG likely promotes a more robust SEI, which contributes to its overall superior performance.

The charge transfer resistance (R_{ct}), which is associated with the kinetics of lithium-ion intercalation and deintercalation at the electrode surface, revealed substantial differences between the two materials. For PG, the R_{ct} increased dramatically after cycling, indicating a degradation in charge transfer kinetics.[44] The observed rise in R_{ct} suggests that the graphite electrode surface may be affected by issues such as poor stability and

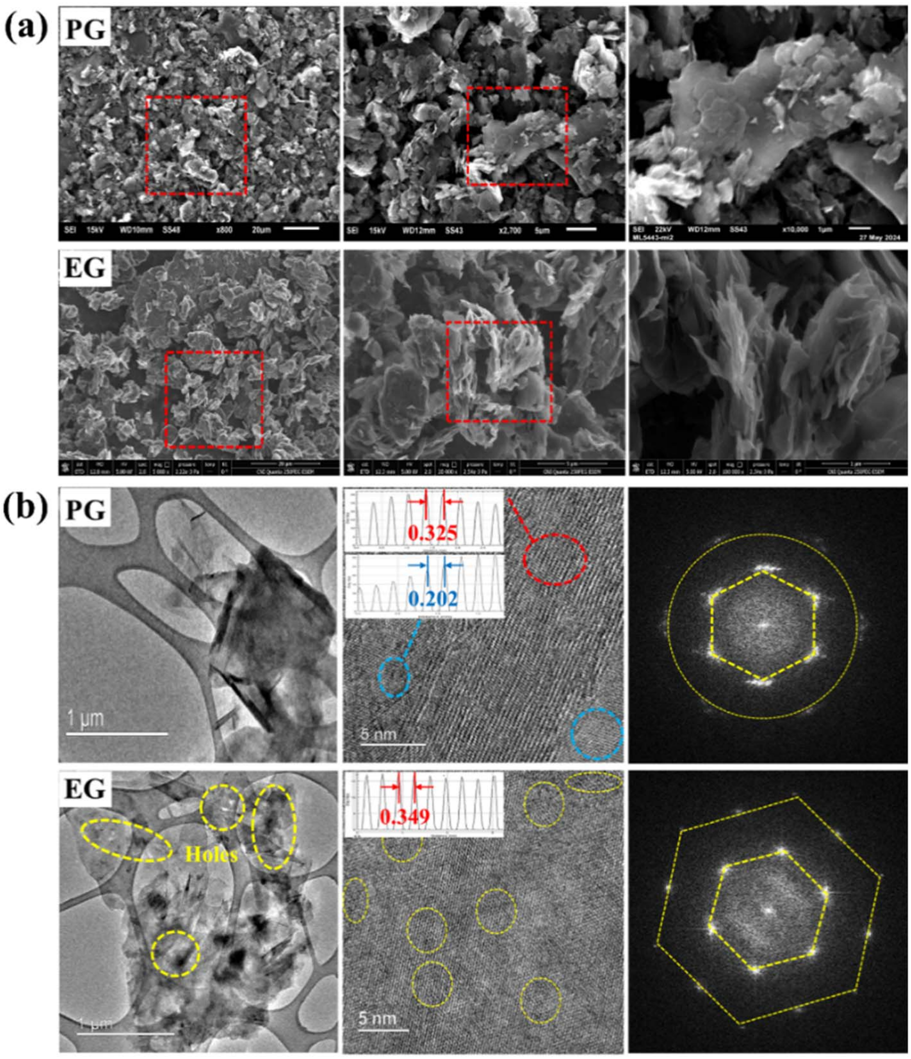

Fig. 3 Morphological evaluation using (a) SEM and (b) HRTEM: PG without modification and EG after surface engineering.

lithium plating/stripping.[45] These factors together impede the efficient movement of lithium ions within the electrode. On the other hand, EG showed a relatively minor increase in R_{ct}. This slight increase highlights the structural and kinetic advantages of EG, as its porous morphology and expanded structure allow for more efficient lithium-ion diffusion and a greater number of intercalation sites,[46] even after repeated cycling,[47] which not only enhances the migration rate of Li^+ ions but also significantly improves the kinetics of the electrochemical reactions.[48]

The lithium diffusion coefficient (D_{Li}) highlights the mobility of lithium ions within the electrode material, which is essential for efficient charge transport and overall battery performance.[49] The calculation of lithium-ion diffusion was performed using the diffusion coefficient and Warburg factor as detailed in the SI. Expanded graphite (EG) demonstrates a significantly higher diffusion capacity compared to pristine graphite (PG), indicating that the material's structure is more conducive to lithium-ion movement. After cycling, while both materials show a decrease in D_{Li}, EG retains a significantly better diffusion capacity than PG, suggesting enhanced structural and electrochemical stability. Additionally, the difference in D_{Li} between the pre- and post-cycling states is smaller for EG, demonstrating its resilience against degradation.

Cyclic voltammetry (CV) measurements were conducted to assess the electrochemical performance of EG and PG as anode materials, as shown in Fig. 4(c) and (d). EG exhibited well-defined cathodic and anodic peaks, indicative of efficient and reversible lithium-ion intercalation/de-intercalation processes. A smaller peak separation in EG compared to PG suggests lower polarization, attributed to improved electrochemical kinetics and reduced energy losses.[50] Additionally, the sharper intensity of the cathodic peaks for EG indicates an enhanced lithium storage capacity and reversibility.[51] These characteristics highlight its higher energy density and the potential for improved performance over extended cycling.

In contrast, PG shows less pronounced redox peaks, indicating slower reaction kinetics and less efficient lithium-ion diffusion.[52] The larger peak separation for PG reflects higher

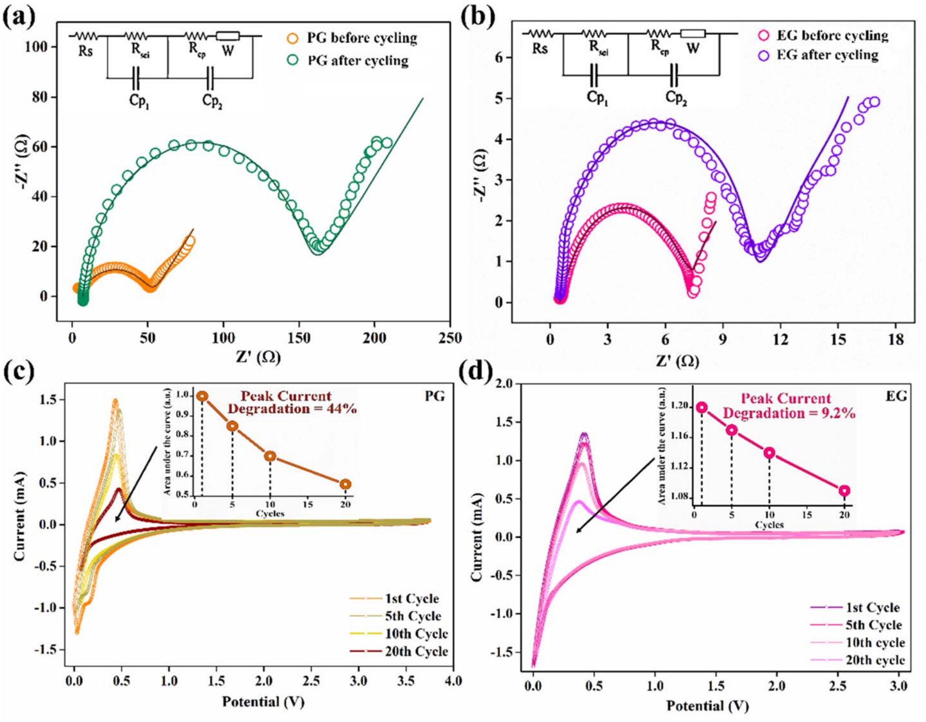

Fig. 4 (a and b) Electrochemical Impedance Spectroscopy (EIS) analysis of PG and EG cells; (c and d) cyclic voltammetry (CV) profiles of PG and EG before and after cycling.

Table 1 Data from the EIS fitting curve

Samples	R_s	R_{sei}	R_{ct}	D_{Li} (cm^2 s^{-1})
PG before cycling	4.00	8.74	33.24	9.60×10^{-14}
PG after cycling	7.31	43.63	99.18	1.77×10^{-14}
EG before cycling	0.43	0.93	6.06	4.19×10^{-13}
EG after cycling	0.57	2.32	7.50	3.01×10^{-13}

polarization, which could stem from structural disorder, defects, or lower crystallinity.

Fig. 5 shows the full cell performance of pristine graphite and expanded etched graphite with the NMC532 commercial cathode at a 0.5C-rate. Fig. 5(a) illustrates how specific discharge capacity and coulombic efficiency change with the cycle number. Initially, the specific discharge capacity of PG is approximately 129.7 mAh g^{-1}, which is lower than that of EG (approximately 179.45 mAh g^{-1}), due to factors such as its low interplanar spacing, sp^3 and sp^2 hybridized carbon structures, and surface area (as confirmed by Fig. 2). Additionally, PG's discharge capacity decreases continuously from approximately 129.7 mAh g^{-1} to below 76.09 mAh g^{-1} after 300 cycles, resulting in a capacity retention percentage of 55.56%. This decrease is accompanied by a significant reduction in coulombic efficiency, which drops below 90%. In contrast, EG demonstrates superior cycling stability, maintaining a higher capacity retention of 89.3% and a greater coulombic efficiency of 93.8% over the same number of cycles. Thus, the expanded etched graphite demonstrates enhanced lithium intercalation and deintercalation capabilities. Due to its porous architecture and stable composition, the continual accumulation of lithium ions during cycling is significantly mitigated, thereby augmenting cycling stability over extended durations.[53] To evaluate the rate performance of the pouch cell prepared using PG and EG as anode, charging–discharging is performed at different C-rates (0.3, 0.5, and 1C), as shown in Fig. 5(b). It is concluded that EG exhibits a higher discharge capacity than PG at all C-rates, with EG recovering well at 0.3C, which is attributed to the porous and exfoliated structure of EG, ensuring fast Li$^+$ transportation and stable SEI formation. Several research studies have investigated surface acid pretreatment techniques; however, our method demonstrated better stability and reduced undesirable reactions that affect the formation of the unstable solid-electrolyte interphase (SEI) layer, as confirmed by Fig. 5(c).

The State of Health (SOH) analysis shown in Fig. 5(d) supports these conclusions. EG maintains about 85% of its original SOH after 300 cycles, while PG experiences a rapid decline, holding on to less than 60% of its initial health because of notable structural weakening.

Fig. 5(e) and (f) depict the voltage profiles for PG and EG over selected cycles (1st, 50th, 100th, 200th, and 300th). In PG, the voltage–capacity curves shift and decrease noticeably with increasing cycle numbers, suggesting significant irreversible capacity loss and structural deterioration. The plateau regions associated with lithium intercalation and deintercalation diminish in prominence, indicating a decline in electrochemical performance kinetics.

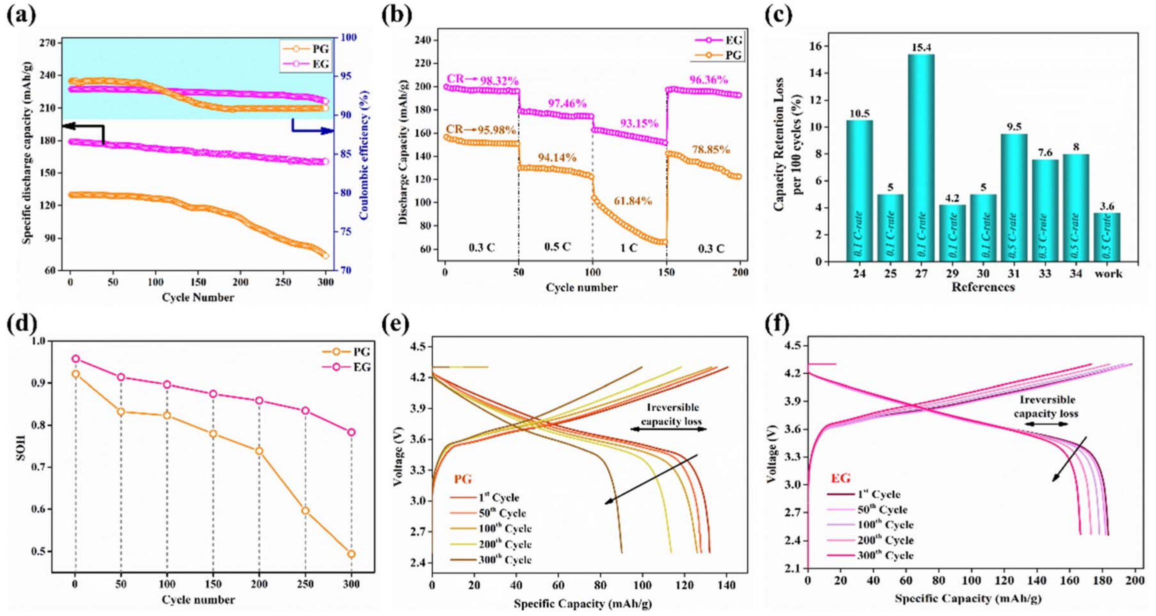

Fig. 5 Full cell performance by (a) cycling performance and coulombic efficiency at 0.5C-rate, (b) rate capabilities at various current rates, (c) comparative study of capacity retention loss per 100 cycles at different C-rates with different acid treatments (other literature), (d) state of health (SOH), and (e, f) charge/discharge profiles of PG and EG.

In contrast, EG shows stable voltage profiles after 300 cycles, with minimal capacity fading and better retention of distinctive plateau areas. The slight irreversible capacity loss in EG highlights its enhanced mechanical strength and improved compatibility with the electrolyte system.

Overall, the comparative electrochemical analysis demonstrates that EG surpasses PG in capacity retention, coulombic efficiency, state of health (SOH) maintenance, and voltage stability, thus establishing it as a more promising candidate for high-performance lithium-ion battery anodes.

3.3 Post-mortem analysis

3.3.1 XPS analysis. The etching process (acid treatment) can alter the diffusion of elements, promote structural evolution, and form a stable surface on graphite particles. The lithiation mechanism of both pristine and expanded etched graphite was examined through X-ray Photoelectron Spectroscopy (XPS) analysis for non-cycled (Fig. S1–S3) and cycled (300 cycles) pouch cells with acid-treated graphite. Fig. 6 shows clear peaks for F, O, and C, indicating structural changes in the graphite after acid treatment. Regarding SEI formation, Li_3PO_4 and LiF are generated through primary precipitation and decomposition of $LiPF_6$ with EC and DEC solvents, as depicted in Fig. 6(a) and (d). During electrolyte decomposition, Li_2CO_3 is mainly produced, as shown in Fig. 6(c) and (f). In the C 1s spectra, peaks at 284.5 eV, 285.2 eV, 286.8 eV, and 290.1 eV correspond to C=C, C–O, C=O, and Li_2CO_3, respectively, as shown in Fig. 6(c) for pristine cycled anode graphite.[54] The C 1s spectra of acid-treated anode graphite show an increased peak for Li_2CO_3 and a decrease in C–O, along with a narrowing of the C–C peak, indicating a more ordered graphite structure and a better-defined sp^2-hybridized carbon network, as shown in Fig. 6(f). Notably, the C=O peak diminishes and broadens in the acid-treated sample after cycling in the C 1s spectra, which enhances surface oxygen groups to improve the anode's electronic conductivity and reduce side reactions with the electrolyte. The surface chemical composition of EG and PG after cycling was analysed using XPS, as shown in Fig. 6(g), focusing on the stability and nature of the solid electrolyte interphase (SEI). The deconvoluted elemental contributions, color-coded, include Li_2CO_3 (yellow), LiF (orange), and Li_3PO_4 (red) as stable inorganic SEI components; C=O (light blue) and C–O (dark blue) as less stable organic species. Notably, EG exhibits a significantly higher proportion of inorganic species, particularly LiF and Li_2CO_3, which are known for their high electrochemical and thermal stability, as well as their ability to form a dense, durable passivation layer.[55] A moderate amount of Li_3PO_4 in EG further supports the formation of a protective SEI. Conversely, PG exhibits higher levels of C=O and C–O groups, indicating a dominance of organic SEI components that tend to be more reactive and less stable over long-term cycling. These findings suggest that EG forms a more stable, inorganic-rich SEI, which helps enhance interfacial stability, limit continuous electrolyte decomposition, and boost electrochemical performance.

Furthermore, XPS analysis showed the presence of Li_2O on the surface of PG (~9.53 at%), while it was nearly absent (~0.21 at%) in EG.[56] This difference is due to the distinct surface chemistries and SEI development pathways of the two samples. C=O and C–O surface groups can be reduced to form Li_2O, either directly or *via* electrolyte decomposition reactions. Additionally, the lower amounts of LiF and Li_2CO_3 in PG suggest delayed or less effective SEI passivation, which allows prolonged electron transfer and further reactions with the electrolyte or

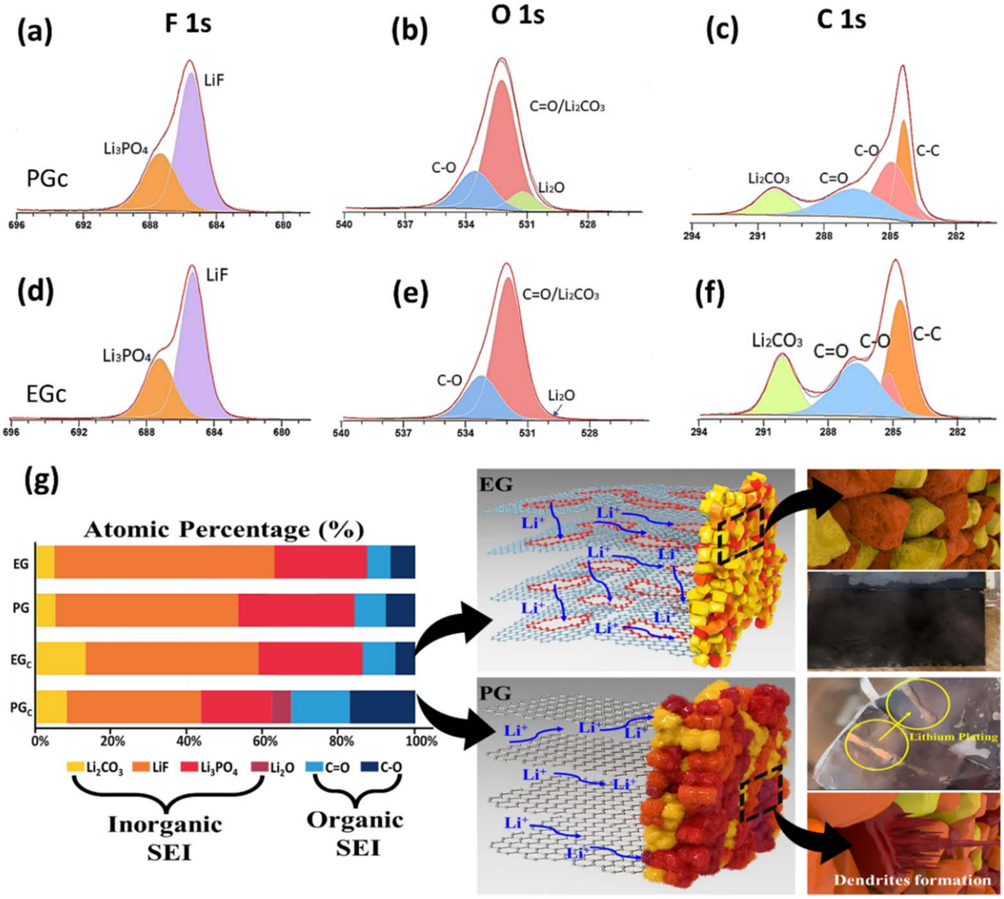

Fig. 6 XPS results (a–f) of the pristine and treated graphite anode obtained from the cells after cycling, including surface chemical composition and (g) atomic percentage of inorganic and organic species of pristine and treated graphite anode.

oxygen-containing species. In contrast, EG forms a more durable inorganic SEI layer rich in LiF, Li_2CO_3, and Li_3PO_4 early on, effectively reducing surface reactivity and limiting Li_2O formation. Although Li_2O is thermodynamically stable, it is mechanically softer and less ionically conductive than LiF, making it a less favourable component of the SEI. Therefore, the presence of Li_2O in PG supports the conclusion that EG has a more stable and protective SEI interface.[57]

As revealed by XPS analysis, the SEI formed on carbonized EG is enriched in inorganic components, in contrast to pristine graphite. The inorganic-rich SEI is thinner, more ionically conductive, and mechanically stable, enabling homogeneous Li^+ flux across the electrode surface. Additionally, structural expansions of the graphite layers improve intercalation kinetics and reduce charge transfer resistance, as indicated by the resulting data and cycling performance (Fig. 5). Increased porosity creates more accessible lithium storage sites, allowing the electrolyte to penetrate deeper and improve contact between the electrode and the electrolyte. This enhances the solid electrolyte interphase (SEI) formation, leading to more stable cycling performance that lowers charge-transfer resistance and enables faster Li-ion exchange. This ground intercalation of functional groups through acid treatment, which is confirmed by XPS and FTIR (Fig. S4 and S5) modified the electrochemical behaviour of graphite, balancing improved lithium-ion accessibility with potential conductivity losses.

Surface energy and surface chemistry changes, confirmed by contact angle and zeta potential, respectively, are presented in Fig. 7(a) and (b) for the anode samples of PG and EG anodes before and after cycling. Contact angle measurements offer deeper insights into the interfacial stability of the electrodes. From Fig. 7(a), it is observed that the pristine PG sample exhibits a relatively low surface energy ($\sim$38 mN m^{-1}), which increases significantly to approximately 72 mN m^{-1} after cycling. This considerable increase indicates substantial surface reconstruction, likely due to electrolyte decomposition and unstable SEI formation, as confirmed by SEM images of the anodes before (see SI, Fig. S7) and after cycling (Fig. 7(c) and (e)). These changes result in volume expansion, cracking, and an increase in surface roughness. The SEI expands (becomes thicker) and becomes less homogeneous, which increases Li-ion diffusion resistance while simultaneously reducing conductivity. This aligns with the fact that cracks lead to electrolyte infiltration, increasing resistance and affecting the cycling stability of the anode layer and the cell overall. Additionally, higher wettability reflects greater electrolyte consumption and capacity fading, leading to lower cycling efficiency.

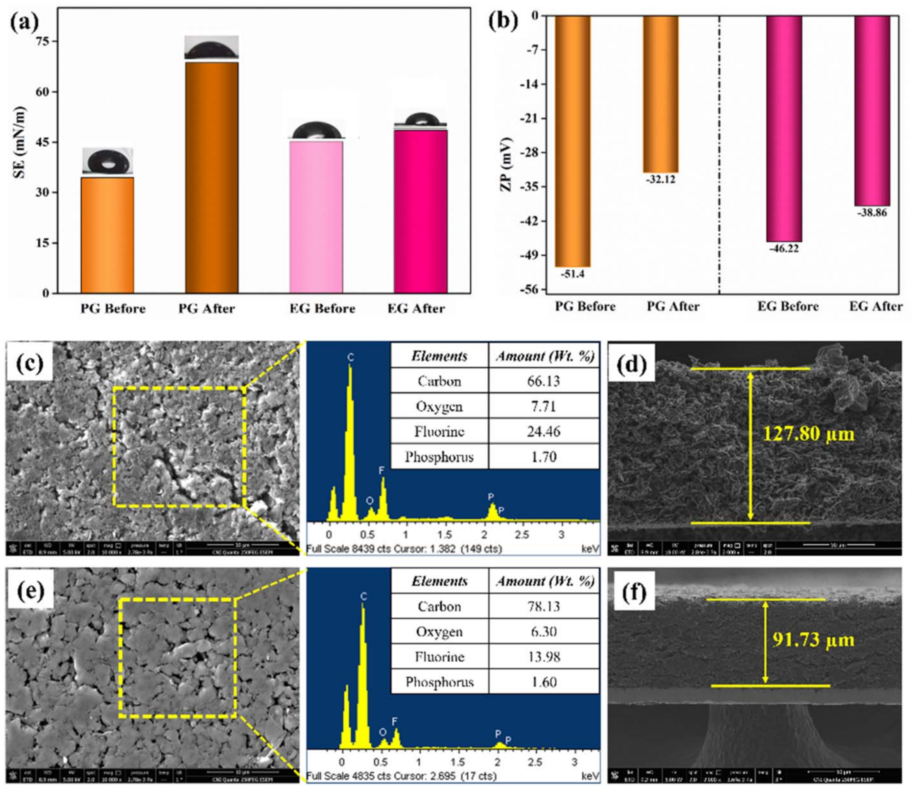

Elements	Amount (Wt. %)
Carbon	66.13
Oxygen	7.71
Fluorine	24.46
Phosphorus	1.70

Elements	Amount (Wt. %)
Carbon	78.13
Oxygen	6.30
Fluorine	13.98
Phosphorus	1.60

Fig. 7 (a) Surface energy measurements; (b) zeta potential analysis of pristine and acid-treated graphite before and after cycling; (c and d) top-view with EDS point scan and cross-sectional SEM images of aged PG anode; (e and f) top-view with EDS point scan and cross-sectional SEM images of aged EG anode.

In contrast, the EG sample starts with a higher surface energy of approximately 50 mN m^{-1} and only experiences a slight decline to around 48 mN m^{-1} after cycling, indicating minimal interfacial degradation. The maintained surface energy in EG suggests the establishment of a robust and stable SEI layer that effectively minimizes side reactions during extended cycling. These findings correlate with the enhanced electrochemical performance of EG, especially its impressive capacity retention and reduced voltage hysteresis, underscoring the significance of interfacial stability in improving cycling durability.

Zeta potential (ZP) measurements, as shown in Fig. 7(b), provide distinctive insights into the surface charge properties and colloidal stability of the electrode materials before and after electrochemical cycling. The zeta potential of the PG anode is extremely negative prior to cycling (−51.4 mV), suggesting a strong electrostatic repulsion and relatively high charge surface density. The ZP changes significantly to approximately −32.12 mV after cycling, indicating that a substantial portion of the surface charge is lost, possibly due to surface decomposition, electrolyte decomposition, or adsorption of decomposition products.[58,59] Additionally, the decline in PG (ΔZP = 19.28 mV) indicates a substantial change in surface chemistry, possibly due to reduced lithium adsorption, which leads to weakened electrostatic repulsion and potentially increased particle aggregation.

On the other hand, the decay of ZP of the EG sample before and after the cycling is compared, and it is found that the ZP value of the EG sample remains stable (−46.22 mV before cycling and −38.86 mV after cycling), indicating minimal change (ΔZP = 7.36 mV) of surface charge during long-term cycling. This stability suggests improved surface passivation and a reduction in the electrochemically generated surface defects or contaminant layers. All things considered, the minor fluctuation of ZP in the case of EG favours speculation about better interfacial contact and a reduced degree of side reactions, consistent with the superior electrochemical performance and surface energy retention. The suspension stability is also confirmed by the particle size distribution which showed enhanced surface area and significant improvement stress tolerance of FG (by 28%) compared to PG, reinforcing its structural and electrochemical stability as shown in Fig. S8.

From the perspective of battery performance, the capacity of EG to maintain a sufficiently negative zeta potential (greater than −30 mV) even following surface modification signifies its enhanced suitability for application in lithium-ion battery anodes, wherein both initial dispersion quality and long-term structural stability are of paramount importance.

Fig. 7(c) and (e) reveal that cracks develop in the PG after lithium intercalation and deintercalation, unlike the EG anode. This observation is supported by the SEM analysis before cycling (Fig. S5), which reveals loose particles and intraelectrode voids that hinder lithium transport while enhancing lithium absorption. In contrast, the porous structure and large interplanar spacing of EG maintain a robust structure without deformation, with a good path for lithium-ion transportation. Electrochemical aging causes a considerable swelling of the negative electrode, as shown in Fig. 7(d) and (f). The thickness of the PG and EG anodes after 300 cycles is measured at 127.80 μm and 91.73 μm, respectively. The increased thickness of the aged pouch cells for PG and EG has risen by 79.3 μm and 43 μm, respectively, compared to the initial thickness of the fresh cells. This dimensional change promotes the mechanical instability of PG, but at the same time EG anode emphasises structural robustness during cycling. The EDS point scan further confirms that the increased atomic percentage of fluorine atoms in PG, which is 1.7 times that of EG, indicates that lithium ions are intercalated and trapped within the graphite layers, thereby reducing the discharge capacity.

4 Conclusion

In conclusion, we successfully synthesized expanded etched graphite through a one-step dual process involving HNO_3 and H_2O_2 etching, followed by NH_4OH alkaline leaching. This integrated approach not only creates nanoscale holes and increases the interlayer spacing but also effectively removes impurities, resulting in a structurally accessible and chemically clean graphite surface. The expanded structure and oxygen-containing functional groups enhance lithium-ion transport and promote stable SEI formation. These nanoscale holes promote lithium-ion intercalation and deintercalation, as evidenced by the lithium-ion diffusion coefficient of 4.19×10^{-13} $cm^2\ s^{-1}$, which is significantly higher than the 9.60×10^{-14} $cm^2\ s^{-1}$ observed for pristine graphite. Electrochemical tests yield excellent results, including a high discharge capacity of 179.45 mAh g^{-1} with a 93.8% coulombic efficiency after 300 cycles at a 0.5C-rate, surpassing that of pristine graphite. Additionally, it retains 93.15% of its capacity after 150 cycles at a 1C-rate, demonstrating strong long-term cycling stability. This impurity-free, scalable, and doping-free method offers a promising pathway for developing advanced graphite anodes for next-generation lithium-ion batteries and high-performance energy storage devices.

Looking ahead, the nanoscale holes in EG can also act as reservoirs for silicon nanoparticles, providing additional lithium storage capacity while cushioning the volume expansion of silicon. Additionally, adding heteroatom dopants like N, B, or P into the holey graphite framework can improve electronic conductivity, surface wettability, and Li^+ diffusion kinetics. Such modifications would enhance the structural stability of the EG, thereby providing a balance between high capacity, rate capability, and long-term cycling stability. Our approach demonstrates its versatility for broader application in advanced carbon– and silicon–graphite composite anodes.

Author contributions

K. R. and V. P.: conceptualization, formal analysis, investigation, methodology, software, validation, writing – original draft, review & editing. O. A. T. D.: data curation, software, validation, writing – original draft, review & editing. M. S. and N. Y.: conceptualization, funding acquisition, project administration, resources, supervision. Colin K.: funding acquisition, resources.

Conflicts of interest

There are no conflicts to declare.

Data availability

Raw data are available from the corresponding authors upon reasonable request.

The authors confirm that the data supporting the findings of this study are available within the article and its supplementary information (SI). Supplementary information is available. See DOI: **https://doi.org/10.1039/d5ta05487g**.

Acknowledgements

The authors thank MITACS (Canada), NSERC Alliance program, and Zentek Ltd for their financial support and in-kind contribution to this project.

References

1 M. Dubarry, C. Truchot and B. Y. Liaw, *J. Power Sources*, 2012, **219**, 204–216.
2 R. Wang, L. Wang, R. Liu, X. Li, Y. Wu and F. Ran, *ACS Nano*, 2024, **18**, 2611–2648.
3 Y. Dong, Y. Chen, Q. Zeng, J. Feng, M. Fang, Z. Shi, J. Liu, Y. Sheng, X. Yue and Z. Liang, *Energy Mater. Adv.*, 2024, **5**, 0113.
4 P. Poizot, S. Laruelle, S. Grugeon, L. Dupont and J.-M. Tarascon, *J. Power Sources*, 2001, **97–98**, 235–239.
5 M. Su, Z. Wang, H. Guo, X. Li, S. Huang, W. Xiao and L. Gan, *Electrochim. Acta*, 2014, **116**, 230–236.
6 C. Mao, M. Wood, L. David, S. J. An, Y. Sheng, Z. Du, H. M. Meyer, R. E. Ruther and D. L. Wood, *J. Electrochem. Soc.*, 2018, **165**, A1837–A1845.
7 Y. Zhou, S. Zhang, Y. Li, Z. Guo and H. Pang, *Matter*, 2022, **5**, 8–10.
8 Z. Kang, Y. Wu, X. Sun, J. Xie, Y. Zhang, Q. Zhang, Y. Cui and J. Luo, *Adv. Mater.*, 2023, **35**, 2209288.
9 C. Liu, Y. Zhao, Z. Chen and Y. Cui, *Natl. Sci. Rev.*, 2025, **12**, nwae433.
10 Y. X. Yao, C. Yan and Q. Zhang, *Chem. Commun.*, 2020, **56**, 14570–14584.
11 S. K. Heiskanen, J. Kim and B. L. Lucht, *Joule*, 2019, **3**, 2322–2333.
12 J. Kim, S. M. N. Jeghan and G. Lee, *Microporous Mesoporous Mater.*, 2020, **305**, 110325.

13 S. Goriparti, E. Miele, F. de Angelis, E. di Fabrizio, R. Proietti Zaccaria and C. Capiglia, *J. Power Sources*, 2014, **257**, 421–443.

14 E. R. Logan and J. R. Dahn, *Trends Chem.*, 2020, **2**, 354–366.

15 L. Li, D. Zhang, J. Deng, Y. Gou, J. Fang, H. Cui, Y. Zhao and M. Cao, *Carbon*, 2021, **183**, 721–734.

16 T. Waldmann, B.-I. Hogg and M. Wohlfahrt-Mehrens, *J. Power Sources*, 2018, **384**, 107–124.

17 X. Yue, Y. Yao, J. Zhang, Z. Li, S. Yang, X. Li, C. Yan and Q. Zhang, *Angew. Chem., Int. Ed.*, 2022, **61**, e202205697.

18 W. Cai, C. Yan, Y.-X. Yao, L. Xu, R. Xu, L.-L. Jiang, J.-Q. Huang and Q. Zhang, *Small Struct.*, 2020, **1**, 2000010.

19 C. Wang, Y. Xie, Y. Huang, S. Zhou, H. Xie, H. Jin and H. Ji, *Angew. Chem., Int. Ed.*, 2024, **63**, e202402301.

20 Y. Li, W. Lv, H. Zhao, Y. Xie, D. Ruan and Z. Sun, *Green Chem.*, 2022, **24**, 9315–9328.

21 J. Guo, S. Jin, X. Sui, X. Huang, Y. Xu, Y. Li, P. K. Kristensen, D. Wang, K. Pedersen, L. Gurevich and D. I. Stroe, *J. Mater. Chem. A*, 2022, **11**, 41–52.

22 X. Ding, Q. Zhou, X. Li and X. Xiong, *Chem. Commun.*, 2024, **60**, 2472–2488.

23 N. Nitta and G. Yushin, *Part. Part. Syst. Charact.*, 2014, **31**, 317–336.

24 D. Ruan, L. Wu, F. Wang, K. Du, Z. Zhang, K. Zou, X. Wu and G. Hu, *J. Electroanal. Chem.*, 2021, **884**, 115073.

25 Y. Yang, S. Song, S. Lei, W. Sun, H. Hou, F. Jiang, X. Ji, W. Zhao and Y. Hu, *Waste Manage.*, 2019, **85**, 529–537.

26 A. D. Jaraa and J. Y. Kim, *Mater. Today Commun.*, 2020, **25**, 101437.

27 X. Ma, M. Chen, B. Chen, Z. Meng and Y. Wang, *ACS Sustainable Chem. Eng.*, 2019, **7**, 19732–19738.

28 Y. Gao, C. Wang, J. Zhang, Q. Jing, B. Ma, Y. Chen and W. Zhang, *ACS Sustainable Chem. Eng.*, 2020, **8**, 9447–9455.

29 Y. Gao, J. Zhang, H. Jin, G. Liang, L. Ma, Y. Chen and C. Wang, *Carbon*, 2022, **189**, 493–502.

30 Q. Chen, L. Huang, J. Liu, Y. Luo and Y. Chen, *Carbon*, 2022, **189**, 293–304.

31 C. Yuwen, B. Liu, H. Zhang, S. Tian, L. Zhang, S. Guo and B. Zhou, *J. Cleaner Prod.*, 2022, **333**, 130197.

32 D. Hou, Z. Guo, Y. Wang, X. Hou, S. Yi, Z. Zhang, S. Hao and D. Chen, *Surf. Interfaces*, 2021, **24**, 101098.

33 S. Natarajan, T. Mae, H. Y. Teah, H. Sakurai and S. Noda, *J. Mater. Chem. A*, 2025, **13**, 4984–4993.

34 J. Yang, E. Fan, J. Lin, F. Arshad, X. Zhang, H. Wang, F. Wu, R. Chen and L. Li, *ACS Appl. Energy Mater.*, 2021, **4**, 6261–6268.

35 Y. Lee, S. M. N. Jeghan and G. Lee, *Mater. Lett.*, 2021, **299**, 130077.

36 J. Jeong, S. Jeon, S. Kim, S. Lee, G. Kim, E. Bae, Y. Ha, S. W. Lee, J.-S. Kim, D.-J. Kim and W.-S. Cho, *Part. Fibre Toxicol.*, 2023, **20**, 33.

37 D. Li, F. Tian, B. Chu, D. Duan, X. Sha, Y. Lv, H. Zhang, N. Lu, B. Liu and T. Cui, *Sci. Rep.*, 2015, **5**, 13447.

38 C.-X. Zhao, C.-Y. Niu, Z.-J. Qin, X. Y. Ren, J.-T. Wang, J.-H. Cho and Y. Jia, *Sci. Rep.*, 2016, **6**, 21879.

39 P. Liu, J. Yang, J. Peng, Y. Tang, L. He and X. Wang, *Energy Fuels*, 2024, **38**, 15797–15806.

40 C. Weisenberger, D. K. Harrison, C. Zhou and V. Knoblauch, *Electrochim. Acta*, 2023, **461**, 142629.

41 J. Guo, Y. Xu, M. Exner, X. Huang, Y. Li, Y. Liu, H. Wang, J. Kowal, Q. Zhang, P. K. Kristensen, D. Wang, K. Pedersen, L. Gurevich, D.-I. Stroe and P. Adelhelm, *Adv. Energy Mater.*, 2024, **14**, 2400190.

42 H. Gong, H. Xiao, L. Ye and X. Ou, *Waste Manage.*, 2023, **171**, 292–302.

43 J. Shin, T.-H. Kim, Y. Lee and E. Cho, *Energy Storage Mater.*, 2020, **25**, 764–781.

44 J. Li, J. Hao, Q. Yuan, R. Wang, F. Marlton, T. Wang, C. Wang, X. Guo and G. Wang, *Carbon Energy*, 2024, **6**, e518.

45 X. Li, Q. Liu, Y. Wang, J. Lin, C. Ji, Y. Yuan, B. Zhao and X. Xiong, *Small*, 2025, 2411104.

46 A. Helaley, H. Yu and X. Liang, *Energy Adv.*, 2025, **4**, 249–261.

47 X. Wang, J. Zhou, H. Wang, J. Zhang, X. Ma, S. Qiu and L. Chen, *Sep. Purif. Technol.*, 2025, **354**, 129329.

48 B. Xing, S. Jiang, S. Yu, B. Dong, Y. Peng, F. Zhang, C. Huo and A. Li, *Synth. Met.*, 2025, **311**, 117813.

49 L. Yue, M. Yu, X. Li, Y. Shen, Y. Wu, C. Fa, N. Li and J. Xu, *Small Methods*, 2024, **8**, 2400183.

50 F. Fathollahi, M. Javanbakht, H. Omidvar and M. Ghaemi, *J. Alloys Compd.*, 2015, **627**, 146–152.

51 J. H. Xu, D. E. Turney, A. L. Jadhav and R. J. Messinger, *ACS Appl. Energy Mater.*, 2019, **2**, 7799–7810.

52 J.-Z. Guo, Y. Yang, D.-S. Liu, X.-L. Wu, B.-H. Hou, W.-L. Pang, K.-C. Huang, J.-P. Zhang and Z.-M. Su, *Adv. Energy Mater.*, 2018, **8**, 1702504.

53 P. Huang, Z. Li, L. Chen, Y. Li, Z. Liu, J. Zhang, J. Luo, W. Zhang, W.-D. Liu, X. Zhang, R. Zhu and Y. Chen, *ACS Nano*, 2024, **18**, 18344–18354.

54 K. N. Wood and G. Teeter, *ACS Appl. Energy Mater.*, 2018, **1**, 4493–4504.

55 D. Sun, J. Li and H. Nie, *Ionics*, 2025, **31**, 177–188.

56 R. Azmi, F. Lindgren, K. Stokes-Rodriguez, M. Buga, C. Ungureanu, T. Gouveia, I. Christensen, S. Pal, A. Vlad, A. Ladam and K. Edström, *ACS Appl. Mater. Interfaces*, 2024, **16**, 34266–34280.

57 S. Pei, J. Zhao, J. Du, W. Ren and H.-M. Cheng, *Carbon*, 2010, **48**, 4466–4474.

58 N. H. Hawari, H. Xie, A. Prayogi, A. Sumboja and N. Ding, *RSC Adv.*, 2023, **13**, 25673–25680.

59 A. Serrano-Lotina, R. Portela, P. Baeza, V. Alcolea-Rodríguez, M. Villarroel and P. J. Ávila, *Catal. Today*, 2023, **423**, 113862.